

# Three-dimensional simulations of X-ray cavities inflated by radio galaxies.

Michael D. Smith<sup>1\*</sup> & Justin Donohoe<sup>1†</sup>

<sup>1</sup>Centre for Astrophysics & Planetary Science, The University of Kent, Canterbury, Kent CT2 7NH, U.K.

Accepted ..... Received ..... ; in original form .....

## ABSTRACT

Vast cavities in the intergalactic medium are excavated by radio galaxies. The cavities appear as such in X-ray images because the external medium has been swept up, leaving a hot but low density bubble surrounding the radio lobes. We explore here the predicted thermal X-ray emission from a large set of high-resolution three dimensional simulations of radio galaxies driven by supersonic jets. We assume adiabatic non-relativistic hydrodynamics with injected straight and precessing jets of supersonic gas emitted from nozzles. Images of X-ray Bremsstrahlung emission tend to generate oval cavities in the soft keV bands and leading arcuate structures in hard X-rays. However, the cavity shape is sensitive to the jet-ambient density contrast, varying from concave-shaped at  $\eta = 0.1$  to convex for  $\eta = 0.0001$  where  $\eta$  is the jet/ambient density ratio. We find lateral ribs in the soft X-rays in certain cases and propose this as an explanation for those detected in the vicinity of Cygnus A. In bi-lobed or X-shaped sources and in curved or deflected jets, the strongest X-ray emission is not associated with the hotspot but with the relic lobe or deflection location. This is because the hot high-pressure and dense high-compression regions do not coincide. Directed toward the observer, the cavity becomes a deep round hole surrounded by circular ripples. With short radio-mode outbursts with a duty cycle of 10% , the intracluster medium simmers with low Mach number shocks widely dissipating the jet energy in between active jet episodes.

**Key words:** hydrodynamics – galaxies: active – galaxies: jets – radio continuum: galaxies

## 1 INTRODUCTION

It is well established that powerful Active Galactic Nuclei are capable of inflating bubbles in the intergalactic and intracluster media. This includes vast cavities created when gas is driven out by powerful radio galaxies. The cavities are observed as depressions in the surface brightness of X-ray emission which encompass the radio lobes. Such cavities are found in diverse cluster environments and surround a variety of radio galaxy types (Carilli et al. 1994; Giacintucci et al. 2011; Pandge et al. 2012; Vagshette et al. 2017; Pandge et al. 2019); with evidence for low Mach number bow shocks being driven into, and capable of supporting, the environment (Wilson et al. 2006; Stawarz et al. 2014). This phenomenon takes on extra significance as we probe the regulatory role it has on galaxy formation through feedback from Active Galactic Nuclei into the cluster gas (Fabian 2012; Hardcastle et al. 2019).

With the advent of new X-ray technology, we can now expect detailed measurements of the structure of these cavities at multiple frequencies. Our main purpose here is to predict how this X-ray structure would appear if the radio galaxy is driven by supersonic hydrodynamic jets. We aim to account for the Mach number, pre-

cession and orientation in order to provide a rich bank of simulated images. The physical properties and radio morphologies have already been published for this set of three-dimensional simulations in Paper 1 (Donohoe & Smith 2016) and Paper 2 (Smith & Donohoe 2019). We thereby wish to probe the implications for the intracluster medium. Specifically, these cavities may provide the link between the regulation of star formation in central massive galaxies and cluster cooling flows. In this respect, we already confirmed in Paper 1 that a high fraction of the jet energy is transferred and dissipated as thermal energy into the intracluster gas.

An X-ray cavity was first associated with the radio source 3C 84 in the Perseus elliptical galaxy NGC 1275 by Boehringer et al. (1993). The Perseus intracluster medium was found to be displaced by the radio lobes although the minimum lobe pressure falls below that of the thermal gas. The brightest regions are located just outside the radio lobes. In addition, the jets appear to change angle from the south-east towards the south with the lobes extending towards the west. While this may indicate jet deflection, it could also be directly related to jet precession. Note that the X-ray ROSAT image is from the soft range between 0.1 and 2.4 keV.

Another X-ray cavity was then associated with the radio galaxy Cygnus A by Carilli et al. (1994). Such X-ray cavities are likely to endure, remaining intact for over 100 Myr, well after the high energy relativistic electrons have cooled within the lobes. Su-

\* E-mail: m.d.smith@kent.ac.uk

† E-mail: jd440@kent.ac.uk,

perimposed X-ray structure can also take the form of ripples, edges, bow shocks and cold fronts (e.g. [Bîrzan et al. 2004](#); [Croston et al. 2011](#); [Shin et al. 2016](#); [Sonkamble et al. 2015](#)).

Numerical simulations of jet-driven radio galaxies have shown that detectable X-ray cavities should surround the radio lobes. A three-dimensional simulation by [Clarke et al. \(1997\)](#) of a straight light jet was used to model Cygnus A. Background subtracted integrations for various energies were presented assuming jet motion in the sky plane. A number of two-dimensional computations by [Hardcastle & Krause \(2013\)](#) of very high Mach number jets confirmed the cavity-shell structures for jets in the sky plane. The X-ray cavities associated with a pair of full magnetohydrodynamic simulations were presented by [Mendygral et al. 2011](#)). Although full two-sided radio galaxies with evolving jet powers were considered in this work, no asymmetries resulted due to the imposed axisymmetric initial conditions. It was found that cavity age and, therefore, cavity power are sensitive to the accuracy of the estimated inclination angle of the jet axis. Cavity age and power estimates within a factor of two of the actual values are possible given an accurate inclination angle. However, even more crucial to the cavity shape is the range of ambient and jet properties. For example, the jet-ambient density contrast is able to generate top-wide, centre-wide and bottom-wide X-ray structures as found in the two-dimensional simulations of [Guo \(2015\)](#) although only the total Bremsstrahlung cooling rate was modelled.

X-ray surface brightness maps were also generated by [Turner & Shabala \(2020\)](#). However, these were based on semi-analytical calculations for mock FR II radio galaxies, enabled after several assumptions including self-similarity and axial symmetry. Although a crude model, this work reminds us that the X-ray emission from distant radio galaxies should become dominated by inverse Compton emission off background photons at high redshifts.

We are now able to perform high resolution three dimensional simulations with sufficient efficiency to systematically investigate the influence of jet dynamics and geometry. This approach will assume a uniform intracluster medium within which the driving galactic nucleus is stationary. We will here study the large-scale X-ray cavities and shocks/edges. We mainly analyse the distribution of the hot gas through thermal Bremsstrahlung radiation but neglect the internal lobe X-rays generated from synchrotron, synchrotron self-Compton and inverse Compton processes. Free-free or Bremsstrahlung radiation generally has a low emissivity and so is associated with the large quantities of hot gas in cooling flows ([Jaffe & Perola 1974](#)).

Synchrotron emission at X-ray energies is detected from within radio jets and hot spots where strong particle acceleration occurs across shock fronts (e.g. [Atoyan & Dermer 2004](#)).

Inverse Compton emission is also deduced from within extended radio jets. In this case, the supply of photons to be upscattered can be produced internally via synchrotron emission, hence the term synchrotron self-Compton. Alternatively, the photons can be from the cosmic microwave background, galaxy starlight or radiation from the active nucleus (e.g. [Wilson & Yang 2002](#); [Kataoka & Stawarz 2005](#)).

We will here also investigate the ability of the radio galaxy to disrupt a cluster cooling flow. To achieve this, we determine the speed of advance of the shock wave that propagates into the cluster environment. Besides the Mach number of the advancing bow shock, it is more relevant to provide the Mach number associated with the temperature jump since that is the observable quantity. For example, [Croston et al. \(2011\)](#) report evidence for a large spheroidal shock in the cluster surrounding the powerful ra-

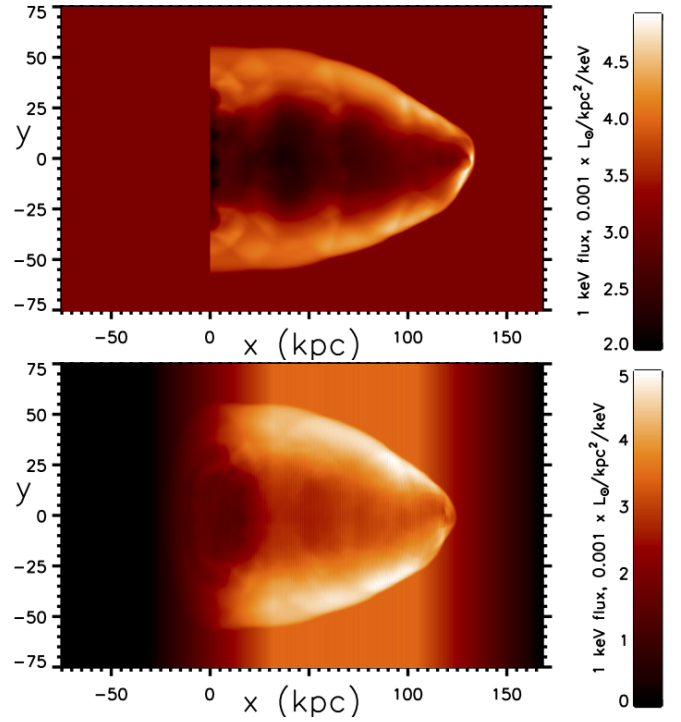


**Figure 1.** X-ray images generated from the data cube for Model ZDA without the uniform background subtraction. The 1 keV emission is displayed for the jet axis in the sky plane (top panel) and  $25^\circ$  out of the plane (lower panel) for jet-ambient density ratio  $\eta = 0.1$ , Mach 6 straight jet with  $1^\circ$  precession angle. This is the free-free X-ray surface brightness; all other images in this paper are sky/background subtracted.

dio galaxy 3C 444. A temperature jump of approximately 1.7 corresponds to a Mach number of 1.7 for a steady hydrodynamic shock. However, [Croston et al. \(2011\)](#) remark that this is likely to be an underestimate since an average over a large region is made.

## 2 METHOD

### 2.1 Simulation and display parameters

The simulations analysed here have been introduced in Paper 1 ([Donohoe & Smith 2016](#)) for their physical attributes and in Paper 2 ([Smith & Donohoe 2019](#)), for their radio morphology and classification. The set of defining parameters and corresponding figures are provided in Table 1.

The analysis was performed with algorithms incorporated into IDL software. Before inspecting the figures, some common properties should be noted in advance (in order to maximise the panel sizes and reduce the caption lengths). The length scales are expressed in kiloparsecs although the pixel unit is 0.5 kiloparsecs which corresponds to the zone sizes of the fixed-grid Eulerian *Pluto* code. Luminosities are in solar units with the total Bremsstrahlung cooling (total), full emission from the specific band per keV (full), and subtracted surface brightness (sub) where the background has been subtracted (not subtracted for the first figure). See Table 2 for a summary.

The simulations were performed with PLUTO, a grid-based code incorporating modern Godunov-type shock-capturing schemes ([Mignone et al. 2007](#)). After comparing the results of numerous options, we chose a fast linear interpolation time-stepping

**Table 1.** Summary of jet properties as expressed for a domain scaled to 150 kpc. The run identification code is consistent with previous papers in this series with the label Z denoting a reflection boundary condition on the injection plane outside the nozzle and the D corresponding to larger  $300^3$  domains.

Figure number	Code used in Paper 1	Jet Mach number	Density ratio $\eta$	Prec. angle	Jet Sound Speed $\text{cm s}^{-1}$	Jet Power $\text{erg s}^{-1}$
1/2	ZDA	6	0.1	$1^\circ$	$3.24 \times 10^8$	$6.42 \times 10^{44}$
3	ZDB	6	0.01	$1^\circ$	$1.02 \times 10^9$	$2.03 \times 10^{45}$
4	ZDC	6	0.001	$1^\circ$	$3.24 \times 10^9$	$6.42 \times 10^{45}$
5	ZDM	6	0.0001	$1^\circ$	$1.02 \times 10^{10}$	$2.03 \times 10^{46}$
6	ZDB	6	0.01	$1^\circ$	$3.24 \times 10^8$	$6.42 \times 10^{44}$
7	ZDB	6	0.01	$1^\circ$	$3.24 \times 10^8$	$6.42 \times 10^{44}$
8	ZDM	6	0.0001	$1^\circ$	$1.02 \times 10^{10}$	$2.03 \times 10^{46}$
9	M2	2	0.1	$1^\circ$	$3.24 \times 10^8$	$2.38 \times 10^{43}$
10	IC	24	0.1	$1^\circ$	$1.02 \times 10^9$	$1.30 \times 10^{47}$
11/12	ZDG	6	0.1	$20^\circ$	$3.24 \times 10^8$	$6.42 \times 10^{44}$
14-xz	ZDG4	6	0.1	$20^\circ$ fast	$3.24 \times 10^8$	$6.42 \times 10^{44}$

(denoted HLLC) scheme as developed by Harten, Lax and Van Leer and detailed by Toro et al. (1994). The simulations were mainly performed on grids of  $300^3$  unless otherwise stated. Hence the voxel and pixel sizes shown in the figures corresponds to 0.5 kpc.

We have performed a resolution study with grids of  $75^3$ ,  $150^3$ ,  $225^3$  and  $300^3$ . We presented results in Paper 1 that showed there was a gradual convergence with  $150^3$  sufficient for most purposes and  $225^3$  providing reliable hot spot properties.

## 2.2 Parameters for the ambient medium

The temperature of the environment is taken as  $T = 4.56 \times 10^7$  K, corresponding to 4 keV, with a hydrogen nuclei density of  $n = 1.21 \times 10^{-3} \text{ cm}^{-3}$  to simulate one half of a Radio Galaxy within a cube which stretches 150 kpc. This is adjustable to other densities and length scales quite easily since the flows are adiabatic with a specific heat ratio of 5/3. It would also be possible to scale the derived emission provided the ratio of the X-ray energy to the temperature were held fixed.

A uniform ambient medium is taken as opposed to the density profiles commonly assumed to model galactic atmospheres such as by Clarke et al. (1997). We model the intracluster medium in this instance but realise that cluster cooling flows and galactic motions would need us to introduce detailed structure.

## 2.3 Parameters for the jet

We configured the code for non-relativistic hydrodynamics. We do this in order to explore ranges in the dynamics in full three-dimensions with a reasonable resolution. Full details were published in Paper 1 for the physical set up and in Paper 2 for the radio emission.

The jet is initially in pressure balance with the ambient medium but the sound speed in the jet is considerably higher given the low density jet which is expressed by the density ratio  $\eta$ . It is important to allow the jet direction to vary, not only to break symmetry but also because there is considerable evidence for this (Krause et al. 2019). Therefore, the jet direction is precessed through sinusoidal velocity changes in the y and z directions as detailed in Donohoe & Smith (2016). The standard slow precession rate has an angular frequency of  $\pi/2$  in units of  $c_s/r_j$  where  $c_s$  is the ambient sound speed and  $r_j$  is the initial jet radius. This corresponds to a precession period of 19.1 Myr with the present units.

## 2.4 Parameters for the emission

To calculate the total Bremsstrahlung emission from the simulations, we assume full ionisation, with 10% helium by number. From the theoretical foundations (Tucker 1975; Rybicki & Lightman 1979), there are a number of approximations for the formula summarised by Yarza et al. (2020) from which we employ

$$L_{\text{brem}} = 1.42 \times 10^{-27} \cdot n_e^2 \cdot T^{1/2} \text{ erg s}^{-1} \text{ cm}^{-3}, \quad (1)$$

where  $T$  is the temperature in Kelvin and  $n_e$  is the electron density measured in  $\text{cm}^{-3}$ .

We present emission maps at soft  $kT_o = 1 \text{ keV}$  ( $2.42 \times 10^{17} \text{ Hz}$ ), intermediate  $kT_o = 10 \text{ keV}$  and hard  $kT_o = 40 \text{ keV}$  X-rays. The formula employed is

$$L_o = 6.8 \times 10^{-38} \cdot n_e^2 \cdot T^{-1/2} \cdot \exp(-T_o/T) \text{ erg s}^{-1} \text{ cm}^{-3} \text{ Hz}^{-1}. \quad (2)$$

Note that we will consider the emission at three specified energies but multiply up to band passes of width 1 keV and provide values per square kiloparsec which generates meaningful luminosities. Scales are provided on bars but are adjusted by appropriate factors as indicated in their titles for display purposes.

## 3 RESULTS

### 3.1 Density dependence

The density of the jet relative to the ambient medium is shown to have a major influence on the X-ray distribution. We define  $\eta$  as the jet-ambient density ratio and consider light jets with  $\eta$  between 0.1 and 0.0001.

With  $\eta = 0.1$ , a substantial depression in the soft X-rays is revealed as displayed in the top panel of Fig. 1. This particular figure is not background subtracted and the data set is confined to within a  $150 \text{ kpc} \times 150 \text{ kpc}$  region filled with  $300^2$  pixels. The display has been chosen so that when the  $300^3$  data cube is rotated (see below), the image will remain in the window with the origin of the jet remaining at a fixed point.

Probably more instructive are the equivalent background subtracted images displayed in Fig. 2. The central cavity is enveloped by a thick elliptical shell. As expected, the highest surface brightness coincides with the leading edge where the heating and compression are strongest. However, the total emission is dominated by the extended flanks which consist of locally shocked gas and adiabatically-expanding hot gas flowing within.

This shell is much dimmer at intermediate X-ray energies

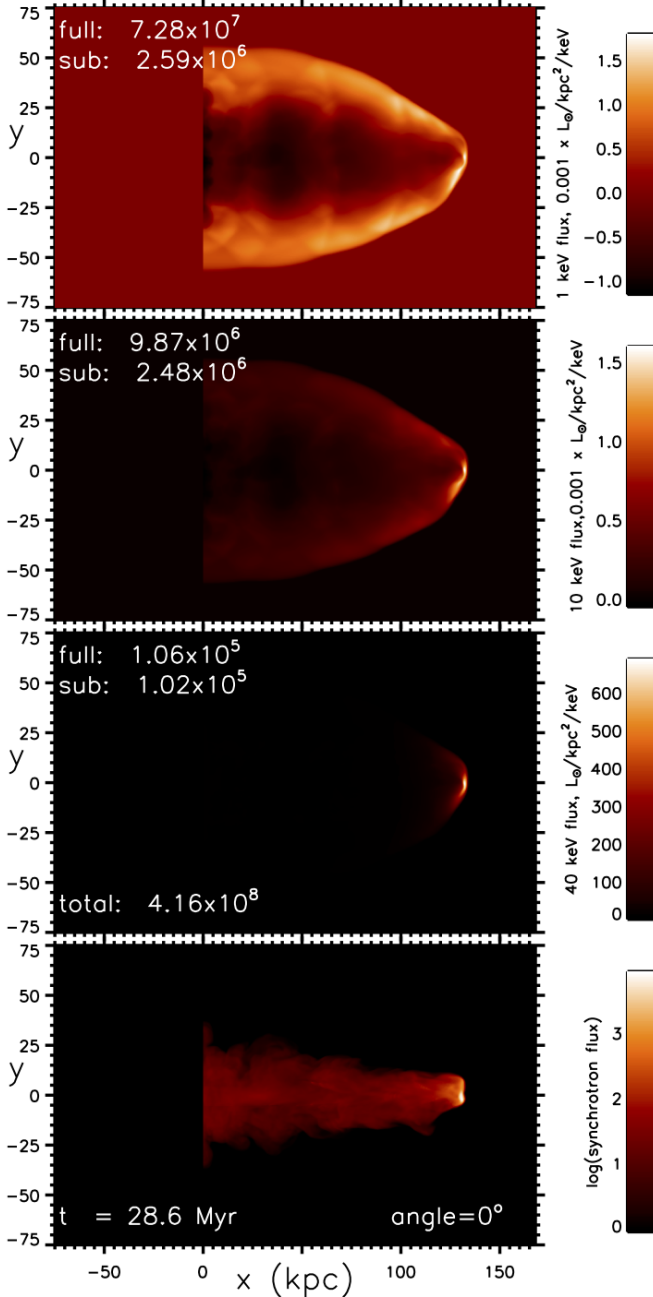


**Figure 2.** Background subtracted images for  $\eta = 0.1$ , Mach 6 jet with  $1^\circ$  precession angle for Model ZDA. The top three panels display the free-free X-ray surface brightness at 1 keV, 10 keV and 40 keV while the lower panel displays a radio image based on a simple synchrotron model. The jet axis is in the plane of the sky.

shown in the second panel while this is then reduced to an arc at hard X-rays in the third panel. It is clear that the hard X-ray energy falls well into the exponential part of the emission function for all except the very hot leading part of the bow. In addition, the elliptical shell is distorted with stronger emission to the 'south' in all bands.

A different structure is apparent for  $\eta = 0.01$  shown in Fig. 3. Firstly, the shell is better described as conical when the jet axis lies in the sky plane. Ribs of emission are now very prominent, running across the shell perpendicular to the jet axis. Four ribs can be seen at

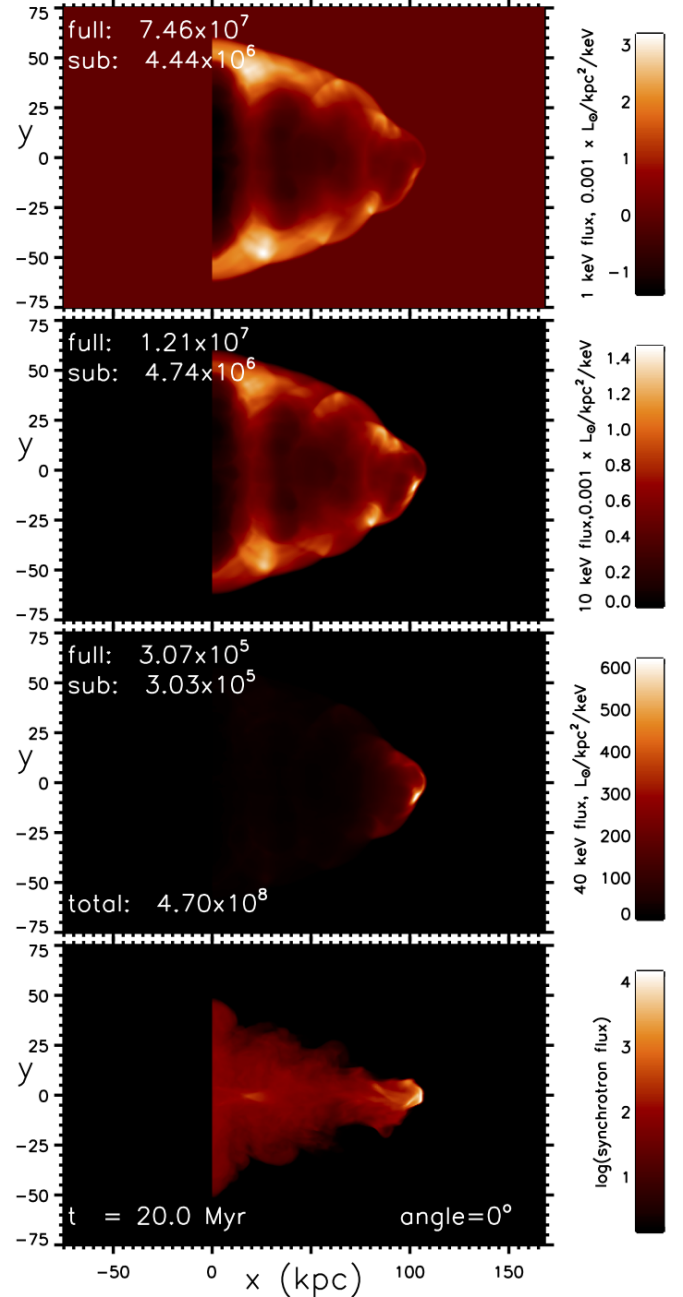


**Figure 3.** Background subtracted images for  $\eta = 0.01$ , Mach 6 jet with  $1^\circ$  precession angle (for Model ZDB). The top three panels display the free-free X-ray surface brightness at 1 keV, 10 keV and 40 keV while the lower panel displays a radio image based on a simple synchrotron model. The jet axis is in the plane of the sky.

the stage shown. The separation between is approximately 60 kpc. The nature of the ribs will be elucidated below through viewing the structure at another angle.

At this lower density, the leading shock is stronger and wider. The jet has penetrated across the grid in a shorter time of 20 Myr, displaying a streamlined structure rather than the blunt appearance of the  $\eta = 0.1$  case above.

With the jet density further reduced, as shown in Fig. 4 and 5, the ribs disappear. Instead, there is a prominent inner cavity in soft X-rays, which is roughly oblate. This is enshrouded by bright



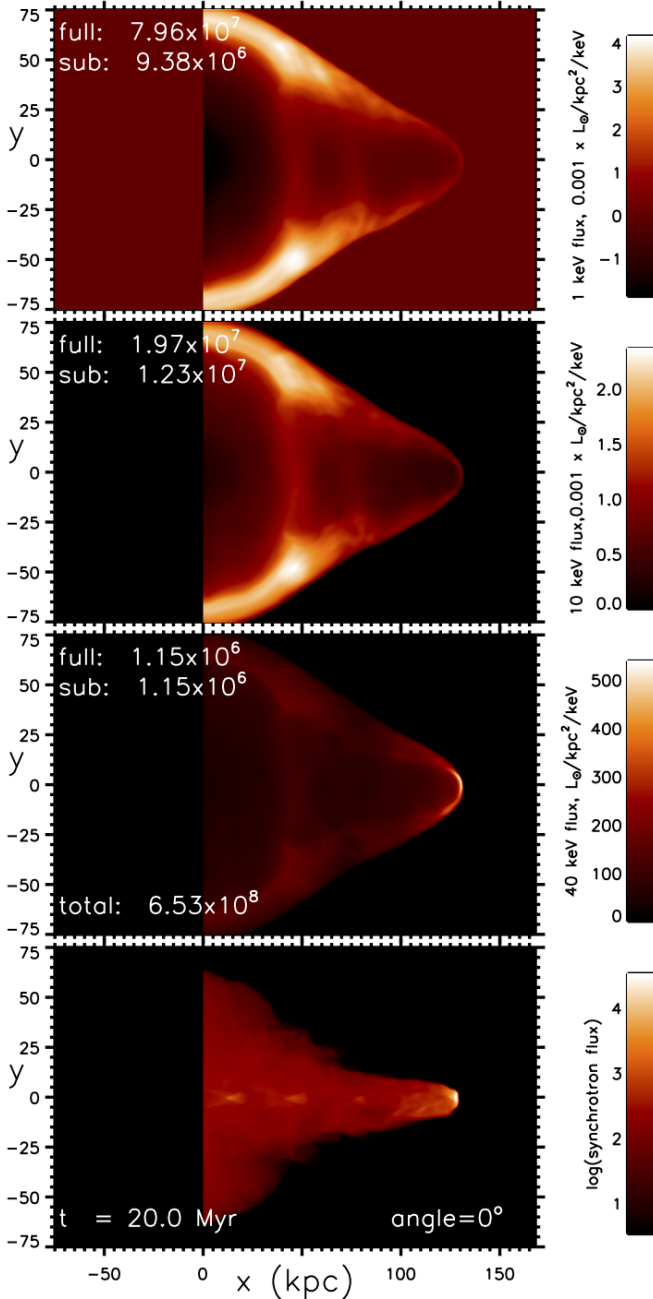


**Figure 4.** Background subtracted images for  $\eta = 0.001$ , Mach 6 jet with  $1^\circ$  precession angle (for Model ZDC). The top three panels display the free-free X-ray surface brightness at 1 keV, 10 keV and 40 keV while the lower panel displays a radio image based on a simple synchrotron model. The jet axis is in the plane of the sky.

shoulders. The visible knotty radio jet now penetrates through the inner cavity although the hot cocoon immediately surrounding it does not seem very distinct. At the lowest density ratio, the entire disturbed region contains two cavities: the inner oblate at all energies and an outer circular bubble at intermediate and hard energies.

### 3.2 Orientation of the jet axis

The integrated line of sight emission with the jet axis at various angles is presented with the panel widths having been chosen so that

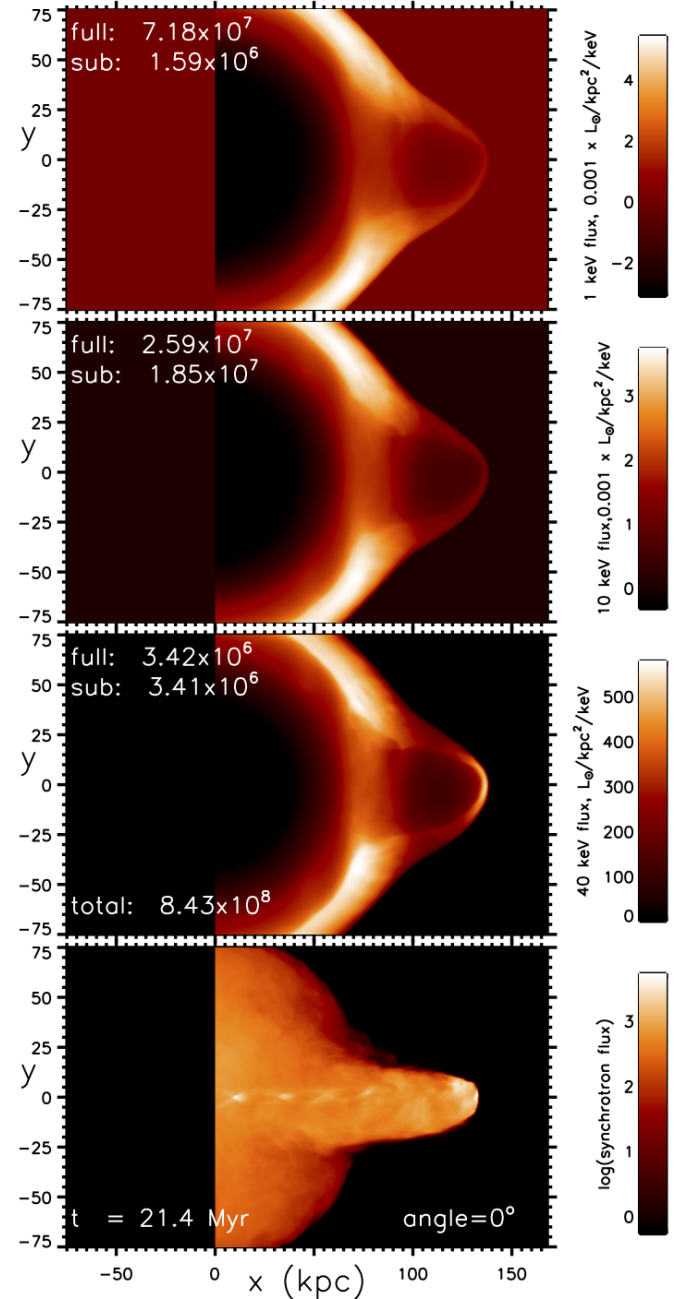


**Figure 5.** Background subtracted images for a very light  $\eta = 0.0001$ , Mach 6 jet with  $1^\circ$  precession angle (for Model ZDM). The top three panels display the free-free X-ray surface brightness at 1 keV, 10 keV and 40 keV while the lower panel displays a radio image based on a simple synchrotron model. The jet axis is in the plane of the sky.

the entire projected data cube is visible and the jet origin remains at a fixed location, the origin (0, 0).

The X-ray structure is altered systematically as the orientation out of the plane of the sky is increased. This effect is illustrated in Figs. 6 at  $25^\circ$  and Fig. 7 at  $75^\circ$ , to the plane of the sky.

At soft X-ray energies, the cone turns into a spindle and the ribs become round ripples. At progressively high energies, the deep cavity becomes smaller and shifts towards the front. Note also that secondary radio hotspots are present at these angles due to projection effects of filamentary structures.

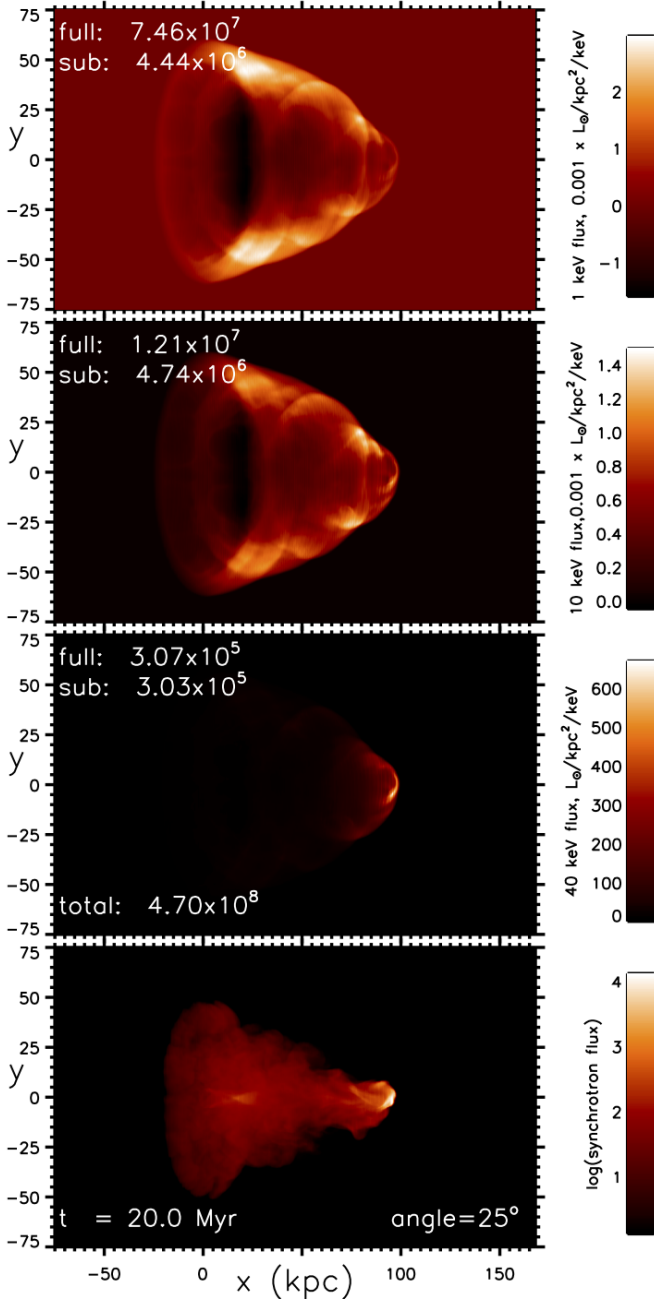


**Figure 6.** The Mach 6 straight jet with the jet axis at an angle of 25° to the plane of the sky. These are background subtracted images produced by a jet with a jet-ambient density ratio of 0.01 and a slow precession with half-angle of 1° (for Model ZDB). The top three panels display the free-free X-ray surface brightness at 1 keV, 10 keV and 40 keV while the lower panel displays a radio image based on a simple synchrotron model.

A remarkable short knotty radio jet is revealed in the lower panel of Fig. 8 for the lowest density jet at a low inclination to the line of sight. This jet is surrounded by an extended radio halo. Moreover, a similar sized thick X-ray front exists at the edge of the halo. Therefore, this simulation may have relevance to a number of quasar jets with halo properties.

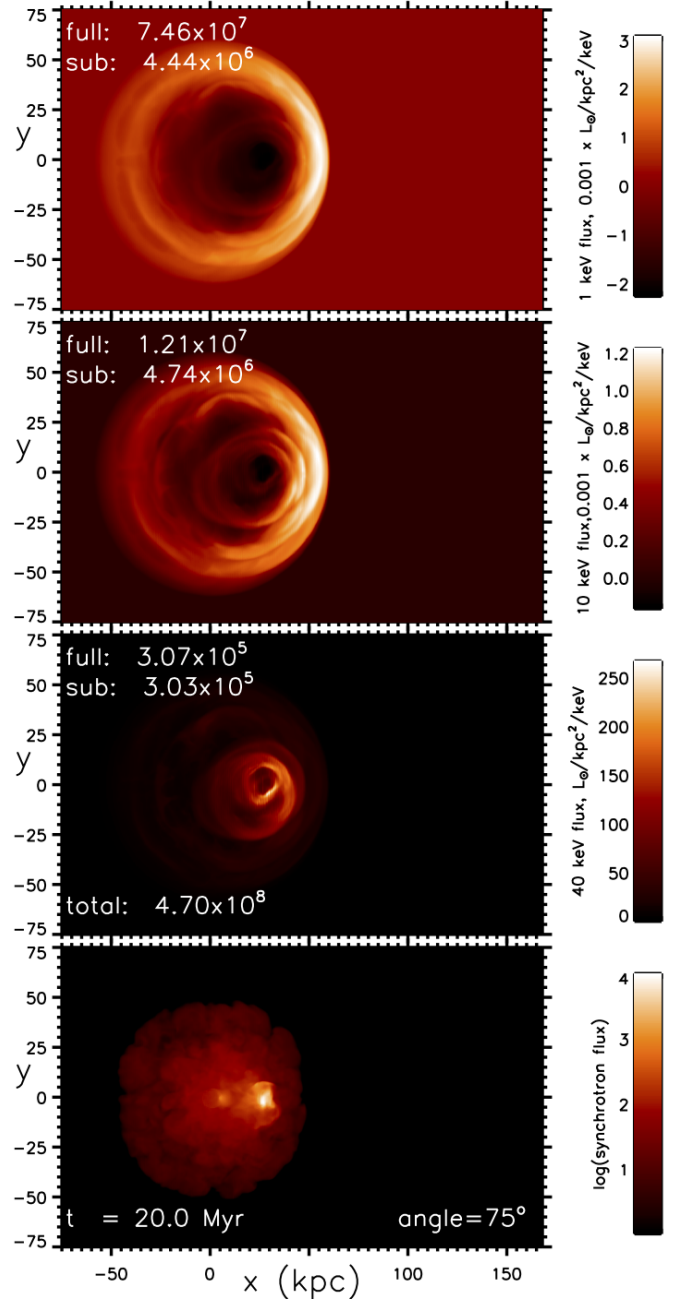


**Figure 7.** The Mach 6 straight jet with the jet axis at an angle of 75° to the plane of the sky. These are background subtracted images produced by a jet with a jet-ambient density ratio of 0.01 and a slow precession with half-angle of 1° (for Model ZDB). The top three panels display the free-free X-ray surface brightness at 1 keV, 10 keV and 40 keV while the lower panel displays a radio image based on a simple synchrotron model.

### 3.3 Jet Mach number

At low Mach numbers, the radio galaxy displays considerable turbulent structure as shown in the lower panel of Fig. 9. Although on these scales the jet has not completely disintegrated, there is no advancing hotspot. The soft X-ray cavity precisely follows the radio lobe. Ahead of the lobe is a very wide and thick shell of enhanced thermal emission. Hence, low Mach number jets can energise a large volume of the intracluster medium.

In hard X-rays, the structure is reversed with only the very

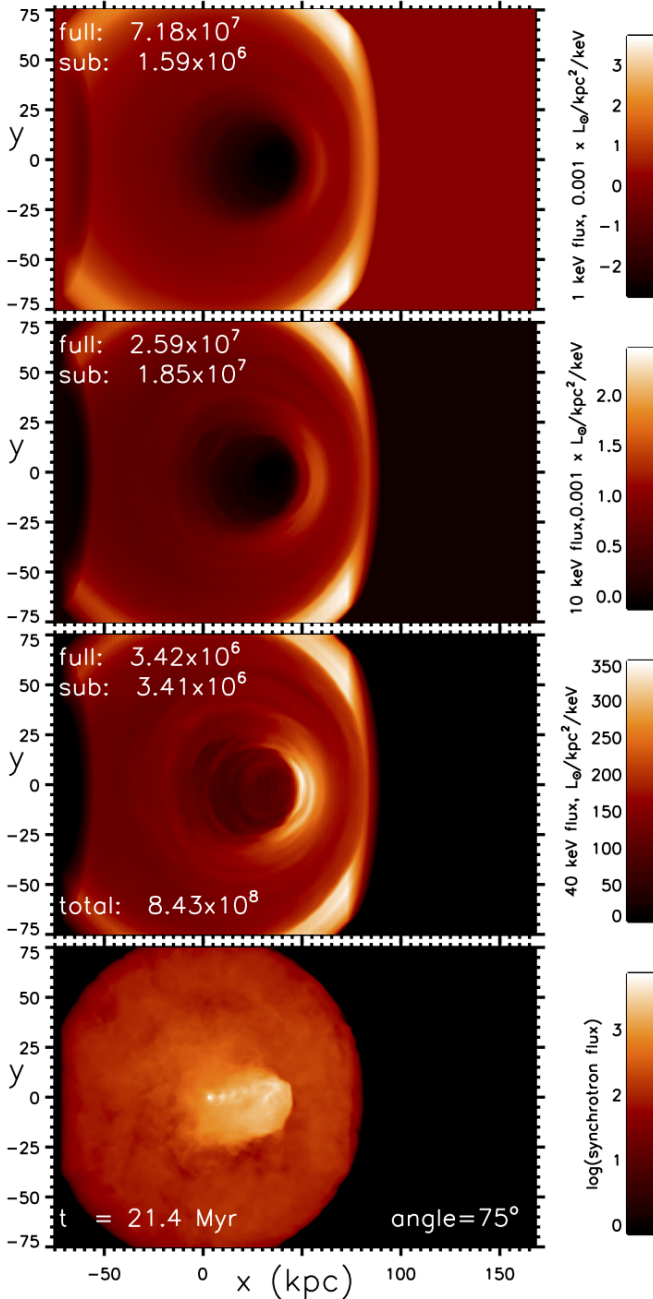


**Figure 8.** The  $\eta = 0.0001$  Mach 6 straight jet with the jet axis at an angle of  $75^\circ$  to the plane of the sky. These are background subtracted images produced by a jet with a jet-ambient density ratio of 0.0001 and a slow precession with half-angle of  $1^\circ$  (for Model ZDM). The top three panels display the free-free X-ray surface brightness at 1 keV, 10 keV and 40 keV while the lower panel displays a radio image based on a simple synchrotron model.

hottest regions contributing. This includes a sheath of hot gas surrounding the jet out to 60 kiloparsec, detected here as two thin parallel filaments. This is followed by a turbulent zone coinciding with the jet disruption. Hence, Bremsstrahlung emission can arise internal to the radio lobes at low Mach numbers, partly due to the stronger dissipation within the radio galaxy and weaker transmission to the intracluster medium (see Column 11 of Table 2).

At high Mach numbers, a contrasting pattern emerges. As

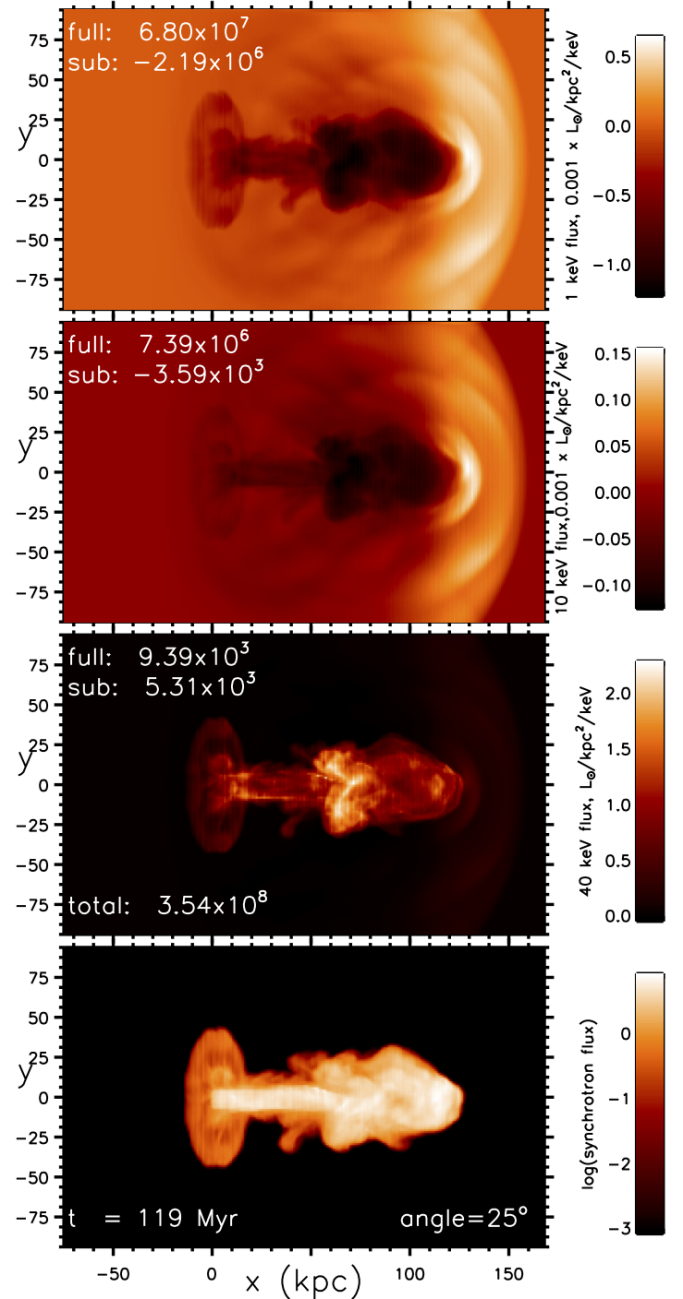


**Figure 9.** A Mach 2 straight jet (fModel M2), viewing angle  $25^\circ$  and  $\eta = 0.1$  with  $1^\circ$  precession. Background subtracted images. The top three panels display the free-free X-ray surface brightness at 1 keV, 10 keV and 40 keV while the lower panel displays a radio image based on a simple synchrotron model. The jet axis is at an angle of  $25^\circ$  to the plane of the sky. The length scales are expressed in kiloparsecs.

shown in Fig. 10 for a Mach number of 24 and  $\eta = 0.001$ , a thimble-like cavity is commensurate with the streamlining due to the high Mach number. This is consistent with the short grid crossing time of 7 Myr. Note that the injected jet is pressure-matched to the environment. That implies that a low-density jet will possess a high sound speed. This compensates in terms of the momentum flow for a given Mach number. Here, however, the advanced speed should be proportional to the Mach number, as indeed found.

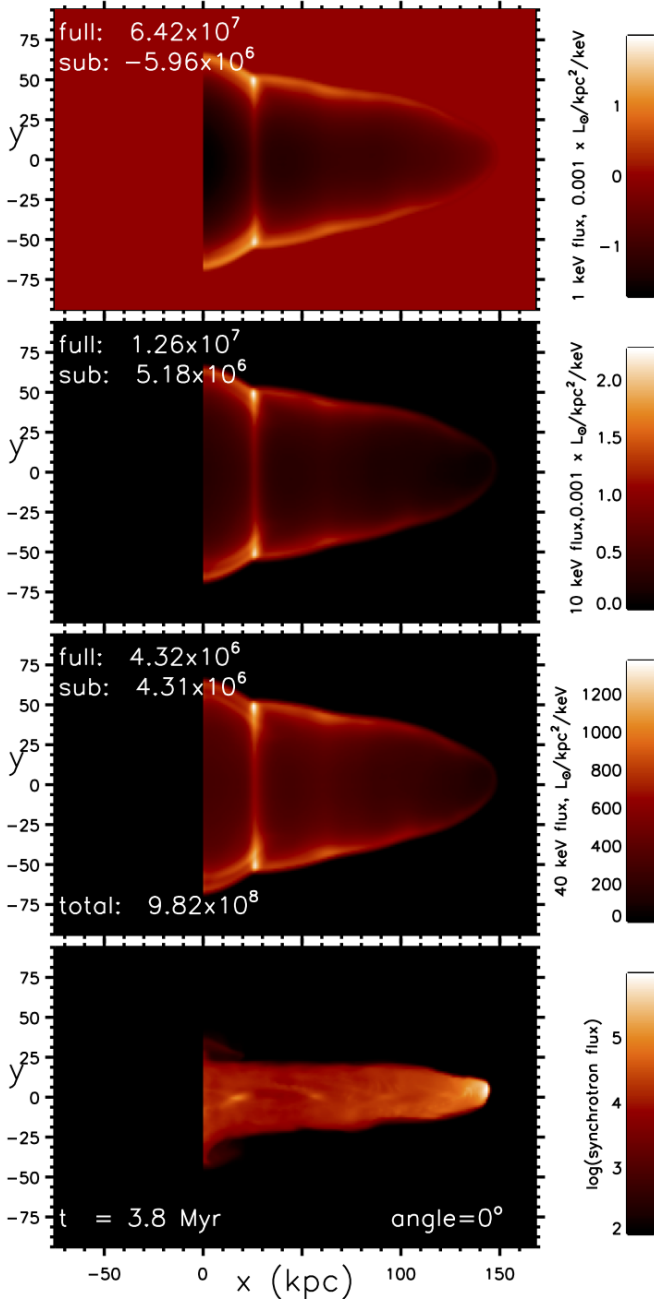


**Figure 10.** A Mach 24 straight jet, viewing angle  $0^\circ$  and  $\eta = 0.1$  (for Model IC). Background subtracted images. The top three panels display the free-free X-ray surface brightness at 1 keV, 10 keV and 40 keV while the lower panel displays a radio image based on a simple synchrotron model. The jet axis is in the plane of the sky.

### 3.4 Precession angle

The Mach numbers for shocks propagating ahead of radio galaxies have been estimated through their X-ray properties. The shocks tend to be very weak with Mach numbers below 3. Moreover, the radio lobes are generally not greatly streamlined. Together, these facts suggest that the speed of propagation into the intracluster medium is only mildly supersonic despite the very high Mach numbers of the driving jets. One way to achieve this in the present context is through a slow precession of the jet axis so that the jet momentum is distributed over a wide surface area.

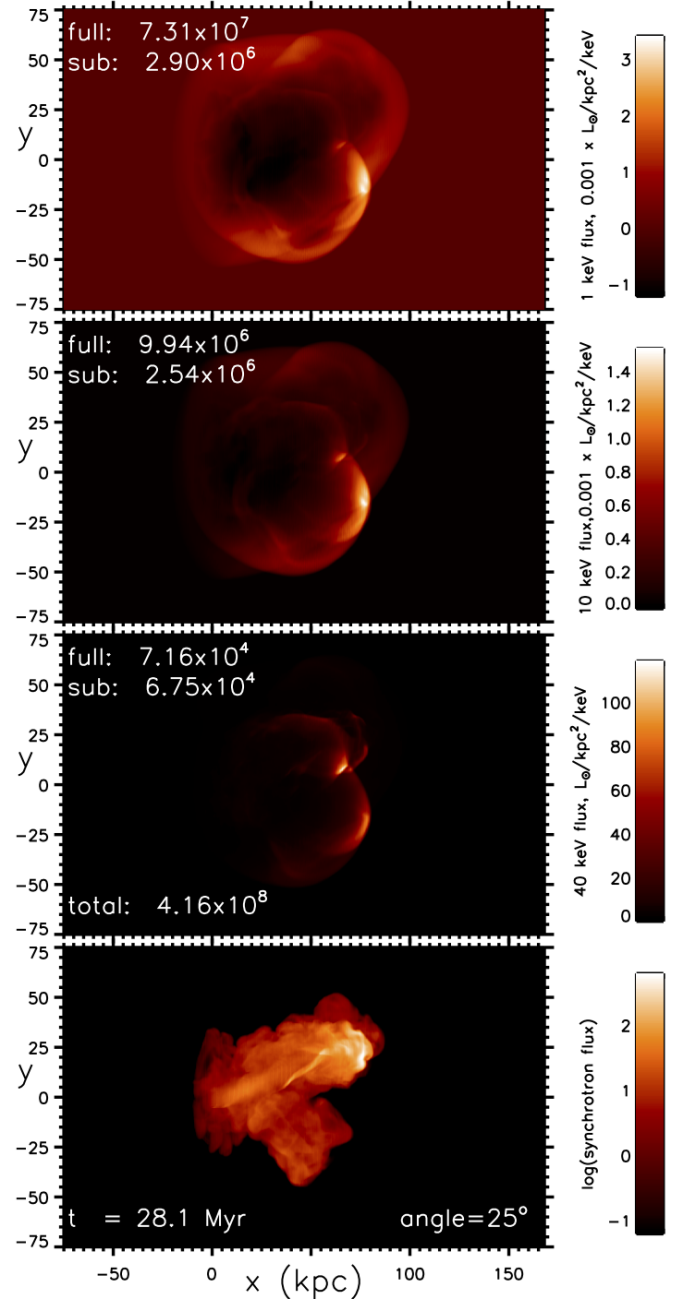


**Figure 11.** A slow precessing jet with  $20^\circ$  precession angle (for Model ZDG). image is from the projected X-Y plane. Images produced by a Mach 6 jet with a jet-ambient density ratio of 0.1. The top three panels display the free-free X-ray surface brightness at 1 keV, 10 keV and 40 keV while the lower panel displays a radio image based on a simple synchrotron model. The jet axis is at an angle of  $25^\circ$  to the plane of the sky.

Precession can manifest itself as multiple radio sub-lobes as shown in Fig. 11, reminiscent of X-shaped or double-double radio galaxies. In X-rays, this simulation has a unique signature: the high surface brightness is associated with the relic radio component rather than with the present hotspot. This holds for the soft and intermediate X-ray energies but the newly advancing lobe is more apparent at hard X-rays. Hence, the Bremsstrahlung emission can remain dominated by the large amount of swept-up and compressed



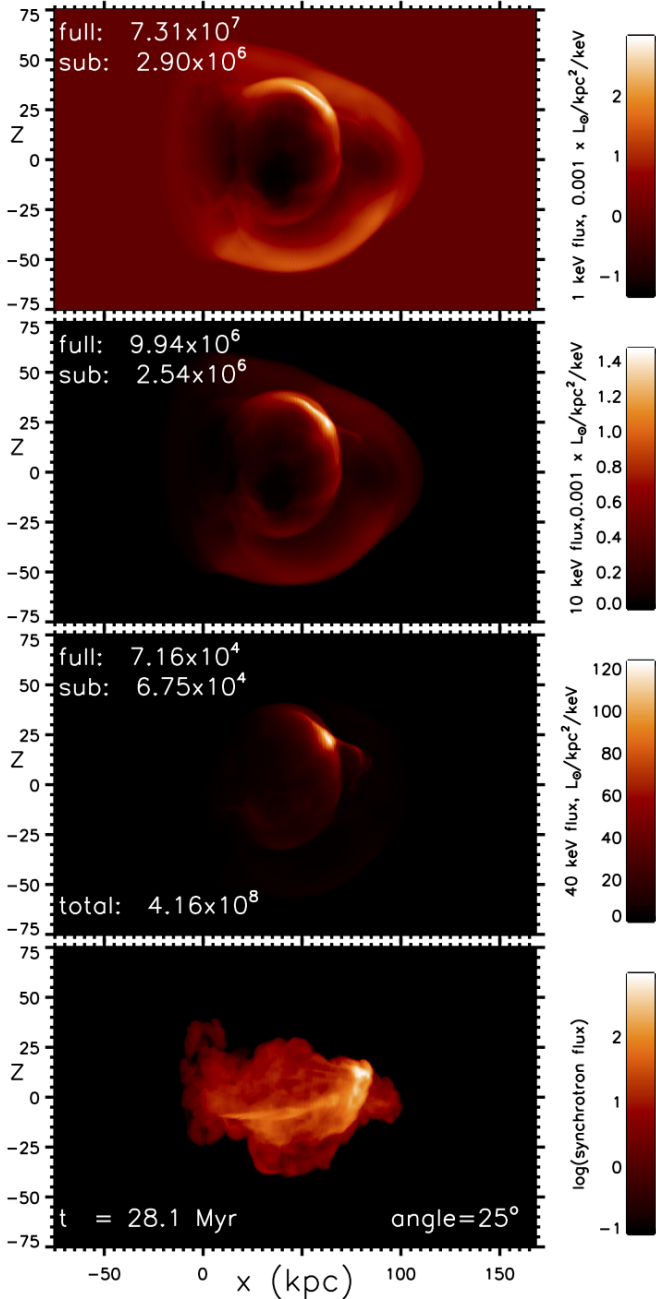


**Figure 12.** A slow precessing jet with 20° precession angle. image is from the projected X-Z plane. Images produced by a Mach 6 jet with a jet-ambient density ratio of 0.1 (for Model ZDG). The top three panels display the free-free X-ray surface brightness at 1 keV, 10 keV and 40 keV while the lower panel displays a radio image based on a simple synchrotron model. The jet axis is at an angle of 25° to the plane of the sky.

material from the previously compressed environment while the jet rotates and progresses through an earlier ejection of lobe material.

Rotated about the jet axis by 90°, yields a contrasting radio morphology as displayed in the lower panel of Fig. 12. The jet begins quite straight and becomes slightly curved before deflection at a secondary hotspot. In this case, the peak soft X-ray emission does not coincide with either hotspot but appears where the over-spill from the primary hotspot has created a new lobe to the top of the image. A further thick rim is present on the opposite side.

On comparison of the two images, it is apparent that there are two circular cavities. The smaller inner cavity corresponds to the region associated with the relic lobe while the large cavity is associated with the overall evacuated lobe.

### 3.5 Luminosity & energetics

The total Bremsstrahlung luminosity is indicated directly on the third panel of the figures. In the absence of the radio galaxy, the luminosity from the 150 kpc cube is  $3.61 \times 10^8 L_{\odot}$ . It should be noted that scaling to a sphere of radius 150 kpc with a hydrogen nuclei density of  $3 \times 10^{-3} \text{ cm}^{-3}$  would yield an X-ray luminosity of  $1.35 \times 10^{10} L_{\odot}$ . Cooling times remain longer than the age of the Universe.

The introduction of the jet increases the total luminosity in all cases despite the cavity formation. The cavity forms through the compression of material, and the shell or rim is generally responsible for enhancing the Bremsstrahlung emissivity. The one exception is the Mach 2 jet in which significant amounts of ambient material have been expelled from the grid.

The total luminosity increases as the jet density is reduced but not by a large factor, approximately doubling over the entire density range of a 1,000. This reflects the fact that a lower density is matched by a higher jet sound speed, which maintains the same momentum flow rate and approximately the same advance speed of the radio hotspot and interface.

Also shown in each panel are the full Bremsstrahlung fluxes in solar units per keV. Underneath this, the background subtracted fluxes are given. This resets the zero point on the colour bar, allowing the cavities to be emphasized as negative values. In this respect, the soft X-ray cavity does deepen as the jet density decreases while, on the other hand, the shell surface brightness increases. Overall, upon background subtraction, the net integrated flux combining enhanced and reduced regions is relatively small. It is also clear that cavities are prevalent in soft X-rays but not in hard X-rays where the background is almost negligible and the emission is mainly generated from the leading edge of the ambient bow shock.

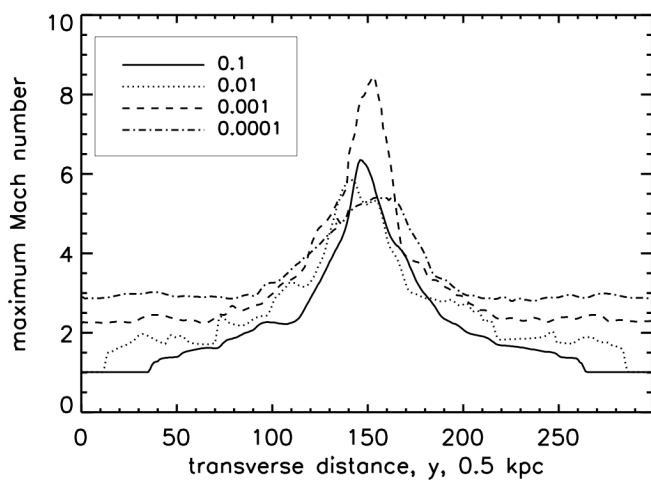
The size and depth of the cavities are quantified and presented in Column 9 of Table 2. The radio lobe area is also listed in Column 8. The detectable lobe is here given a threshold of 1% of the peak value. Hence the radio lobe and the cavity area both generally increase as the jet-ambient density ratio decreases. It can also be noted that the radio area and cavity area can greatly depend on the viewing angle. The depth of the X-ray cavity is measured as the total surface brightness of the cavity within the area, defined as 0.3 below the background in the figures. It is evident that cavities are deeper when the jet axis is closer to the line of sight. However, several factors contribute. For example, the high Mach number straight jet has blown a deep cavity although the streamlined shape means that it has not vacated a large volume. On the other hand, the low Mach number jet has also cleared a deep cavity coincident with the radio lobe.

### 3.6 Intracluster shock Mach number

There are several useful Mach numbers that can be derived from the simulations. The first is from the physical properties. Here, we present the values for the time-averaged Mach numbers along the jet axis which are easily derived for both the interface and the shock front running ahead of it. These are listed in Columns 6 & 7 of Table 2. Note that these are generally high values but appropriate for

**Table 2.** Properties of X-ray images of simulated radio galaxies.

Fig.	Mach number	Density ratio $\eta$	Prec. angle	Angle to sky plane	Interface Mach No.	Bow Mach No.	Radio area kpc <sup>2</sup>	Cavity area kpc <sup>2</sup>	Cavity depth $L_X/10^6 L_\odot$	Energy transfer	X-ray Temp. 10 <sup>7</sup> K	X-ray Mach No.
1/2	6	0.1	1°	0°	4.35	4.48	142	4,592	-1.99	0.71	5.23	1.12
3	6	0.01	1°	0°	5.22	5.42	214	4,634	-2.11	0.86	6.00	1.30
4	6	0.001	1°	0°	6.10	6.29	464	4,187	-2.91	0.92	7.48	1.60
5	6	0.0001	1°	0°	5.89	6.18	10,292	6,940	-15.78	0.94	10.25	2.09
6	6	0.01	1°	25°	5.22	5.42	380	4,533	-2.42	0.87	6.00	1.30
7	6	0.01	1°	75°	5.22	5.42	543	4,575	-5.00	0.87	6.00	1.30
8	6	0.0001	1°	75°	5.89	6.18	15,785	11,745	-8.03	0.94	10.25	2.09
9	2	0.1	1°	25°	1.07	1.19	5,740	19,348	-4.34	0.59	4.71	1.01
10	24	0.1	1°	25°	35.50	37.25	2,765	8,566	-6.83	0.86	6.40	1.38
11-xy	6	0.1	20°	25°	0.80	3.30	3,024	3,769	-2.02	0.79	5.23	1.13
12-xz	6	0.1	20°	25°	0.80	3.30	1,960	3,989	-1.99	0.79	5.23	1.13
14-xz	6	0.1	20° fast	50°	1.44	2.37	7,217	6,532	-5.79	0.82	5.50	1.19

**Figure 13.** The Mach number of the bow shock in the cluster environment as derived from the maximum jump in pressure taking steady shock jump conditions. The value is derived along each y-zone in the z mid-plane.

estimating source ages. The bow cap is typically just 4–5% ahead of the interface apart from the Mach 2 jet which has a 1% stand-off and the anomalous precessing jet which appears as two distinct off-axis lobes encompassed by a surrounding large-scale bow.

The Mach number attributed to the shock driven into the cluster medium can be derived from spectral measurements in the X-ray bands. One measure of the Mach number is calculated from the ratio of X-ray emission in the 1 and 10 keV bands. This generates an X-ray temperature which can be compared to that expected from the jump conditions for a hydrodynamic shock. These values, listed in the final column of Table 2, are very low since the extended low Mach number flanks of the bow dominate.

It can be concluded that the derived Mach number depends on the resolution. This is demonstrated in Fig. 13 where shock hydrodynamic jump conditions have been employed to convert the maximum change in temperature or pressure along the x-axis into an equivalent Mach number for a steady shock. While a temperature jump may be measured observationally, in numerical simulation with an extreme density contrast, the pressure provides a better solution. This figure demonstrates that any observation of the curved bow will be strongly dependent on the spatial resolution. Therefore, extreme caution must be applied when using derived Mach numbers to deduce radio galaxy energetics or dynamics.

### 3.7 Evolution of X-ray flux density

Can we identify candidate X-ray cavities from the total emission in the ambient medium? To determine this, we calculate the total Bremsstrahlung emission from the data cubes in the soft, medium and hard X-ray bands. Moreover, by presenting the time evolution, we gain a further potential diagnostic of radio galaxy age.

Figure 15 shows that the total X-ray emission in each band increases despite the reduction within the cavity. This applies to all bands and is a result of the density squared dependence of the emissivity. Hence, when the radio lobes sweep up the material, they create significant density variations out of the ambient medium while the total mass remains unaltered. Therefore, the local depression is more than compensated by the enveloping region of enhanced emission.

This increase in total emission is mostly detectable in the harder bands. At 40 keV, there is minimal emission before the jet is initiated and the emission strongly increases due to the direct impact. In this case, the emission is sensitive to the rise in temperature across the impact region.

As the source ages, ambient material is ejected from the grid. This was found in the simulations with very low jet densities, as shown by the turn over in the emission curves. This is due to the large lateral expansion of the cavity. On the other hand, although a wide radio source is created in the case of a high jet precession angle, the X-ray emission is not significantly increased in comparison to the straight jet with  $\eta = 0.1$ . We thus conclude that for the enhancement in integrated X-ray emission from the Bremsstrahlung process, the jet density is the crucial factor.

## 4 DISCUSSION

A major result is that the cavity morphology is a function of the jet-ambient density ratio. Note that this treats the jet Mach number and jet-ambient pressure ratio as the two other independent variables. We study here only the pressure-matched case and, for a fixed Mach number, this implies a constant momentum flow rate independent of how light the jet is. The pressure balance condition might be critical to the jet stability and will be relaxed in a follow-up study. Here, we find that for  $\eta = 0.1$ , an ellipsoidal cavity demarcated by a shocked shell appears as an elliptical X-ray cavity and bright shell. As shown in Fig. 1, the shell is typically 20%–25% thick and is likely to be asymmetrical, ultimately caused by a preferred direction of deflection of the jet in the leading impact region.

These cavity results differ from those of Guo (2015). A com-

parison is difficult since their simulations are two dimensional, involve viscosity and consider subsonic jets that generate top-wide cavities. The main difference, however, is that their simulations only considered cavities well after the jet had been switched off, allowing a buoyant bubble to rise in a galactic potential.

As  $\eta$  is reduced in the simulation sequence, the shell shape becomes progressively more conical with the high surface brightness regions located further into the flanks. Most remarkable is the appearance of ribs which cut across the cavity when the jet is in the plane of the sky. The ribs show up as distinct brightenings along the shell and finally as ripples at viewing angles close to the line of sight (fig. 7). This indicates that the structure is caused by oscillatory motion in the impact zone which has been known to experience periodic vortex shedding associated with periodic transitions between double hotspots and single hotspots on the axis (Smith et al. 1985). The shed vortex feeds back on to the approaching jet, squeezing it before the gas is shocked at the hotspot. The shedding time scale is estimated to be the hotspot radius divided by the ambient sound speed. This yields four complete cycles for the  $\eta = 0.01$  simulation, which is consistent with the simulated structure. This is confirmed through closer inspection of the radio image in the lower panel of Fig. ?? which displays previously shed vortices on both sides of the radio cocoon, corresponding to the location of the X-ray ribs.

Enhanced X-ray structure within the Cygnus A thermal cocoon has been identified by Smith et al. (2002) as belts. With *Chandra* data, the description was refined to cross-cutting thick ribs which appear to be wrapped on the inside of an ellipsoidal shell (Duffy et al. 2018). It is certainly reasonable to associate the observed ribs with the rib cage which occurs naturally in these simulations with the minimum of necessary ingredients. Further examples would be expected as we gain high resolution data for other classical doubles.

For the lightest jets, the shell develops wide shoulders on the flanks and a deep ovoid cavity. The radio jet penetrates through the cavity and propagates across the domain. These X-ray attributes are very similar to those associated with 3C 444 (Vagshette et al. 2017) and 3C 320 (Vagshette et al. 2019) which possess double inner cavities with an adjacent rim plus outer shocks.

Radio galaxies generated by jets within a wide precession cone would extend the lateral reach of feedback into the intracluster medium. This is evident from the low Mach number of the shocks into the cluster environment for the  $20^\circ$  precession angle cases in Table 2. However, the fraction of jet energy transferred into the surroundings remains at a substantial level. Therefore, precession does not actually help to increase external support but may help spread this support of the gas across an entire cooling flow (Riffel et al. 2019) and so inhibit galaxy growth, two major issues recently summarised by Hardcastle et al. (2019). Precession may prove to be a prominent dynamical mechanism in distant radio galaxies as they form in proto-clusters. Therefore, we concentrate below on the effects of precession and the influence this may have on their apparent morphological classification.

The dynamical times of the simulated radio galaxies are significantly shorter than the lifetime of a hot dense cooling cluster flow. This would indicate that the present active phase of an AGN would not be directly responsible for the onset of measurable feedback and increase of entropy in the cluster gas (Belsole et al. 2007). Hence, it may be crucial to study how an environment responds after a radio galaxy power supply has been switched off. Indeed, cavities without enveloping shock waves are observed which suggest multiple episodes (Choi et al. 2004) with shock decay in between.

An excellent template for an observed X-ray cavity and shell belongs to the environment of the fat double FR I 3C 310 (Kraft et al. 2012). It is a prime candidate for a radio galaxy formed by a fast precessing jet which has been able to draw out the radio hotspot into a ring in the southern lobe and a broken round arc in the northern lobe. In this case, the energetics have been clearly outlined by Kraft et al. (2012). The X-ray cavity and radio galaxy are powered by an ongoing outburst releasing thermal energy into the gas within the shocked inner 180 kpc of  $10^{61}$  ergs and which emits  $\sim 2 \times 10^{43}$  erg s $^{-1}$  while the outburst energy is  $\sim 10^{61}$  ergs. The Mach number of 1.9 for the expansion is derived from a model for the shock density jump. While these numbers are highly uncertain, this leads to an estimated time-averaged outburst power of  $2 \times 10^{45}$  erg s $^{-1}$  and suggests that the AGN could easily support the cooling flow with a duty cycle of just 10%.

Here we employ our model for the radio emission of a fast precessing jet. The jet has a  $20^\circ$  precession angle and a period of one quarter of the above standard models (i.e. a period of  $r_j/c_s$  where  $r_j$  is the jet radius and  $c_s$  is the ambient sound speed. Figure 14 displays a fat radio lobe with a ring-like structure in the lobe apparent for this angle to the line of sight. The total X-ray power of the simulation of  $2 \times 10^{42}$  erg s $^{-1}$  and jet power of  $6.4 \times 10^{44}$  erg s $^{-1}$  for this one half of the radio galaxy within the 150 kpc cube compares favourably without any need for parameter manipulation. Note the outburst age of 48 Myr and a derived time-averaged Mach number of the leading edge of 1.44 for the interface and 2.37 for the disturbed ambient medium. These values are commensurate with those derived from the jump conditions which yield a maximum Mach number of 2.15. Note that this simulation was performed with extensions in the form of a staggered grid beyond the uniform displayed portion.

X-ray cavities can take many forms and provide a means of investigating galaxy and cluster formation at high redshift since cluster cooling flows are strong X-ray sources. MACS J1447.4+0827 ( $z = 0.3755$ ) provides a recent example of jet evacuated cavities (Prasow-Émond et al. 2020). Unlike Cygnus A, in this case two separate cavities on a scale of 100 kpc are detected. Moreover, the cavities appear to open out away from the central galaxy. While this may be simulated here, the strong emission from the soft X-ray band occurs on the inner section of each side of the source. Thus we do not reproduce the distinct double cavity. This may well be remedied in simulations with, for example, ellipsoidal density profiles. On the other hand, the double X-ray cavity associated with the Phoenix galaxy cluster studied by (Akhori et al. 2020) consists of two well defined depressions that suggest an interpretation in terms of a low Mach number jet such as shown in Fig 9.

A number of cavities at low redshift do possess a double bubble structure with the LoFAR telescope revealing the driving radio galaxy (Birzan et al. 2020). Examples are A1361 and MS0375). The single ovoid or thimble structures predicted here from the high Mach number jets are also found in this survey (e.g. A2052, Zw8276) although less definitive. There is thus the indication that double bubbles are associated with samples derived from cluster surveys while ovals will be found in association with powerful radio galaxies.

A cluster evolution scenario in which AGN feedback regulates the intracluster medium and so controls the development of central galaxies has received much favourable attention (Fabian 2012; Hardcastle et al. 2019). Here, we find quantitative support for the radio-mode in which jet-induced outbursts provide repeated heating events in the environment (Gupta et al. 2020). Although we find that the jet power is effectively transferred into the cluster gas, one

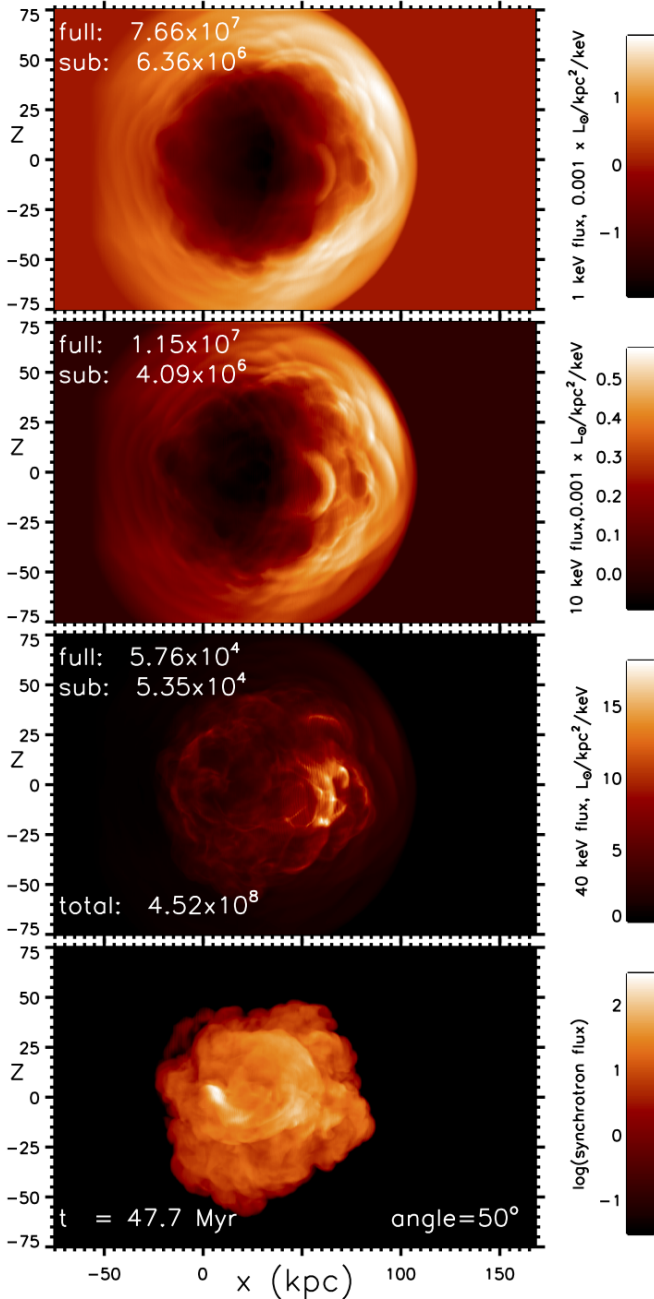


**Figure 14.** A fast precessing Mach 6 jet with  $20^\circ$  precession angle (for Model ZDG4). This image is from the projected X-Z plane. The jet-ambient density ratio is 0.1. The top three panels display the free-free X-ray surface brightness at 1 keV, 10 keV and 40 keV while the lower panel displays a radio image based on a simple synchrotron model. The jet axis is at an angle of  $50^\circ$  to the plane of the sky.

10–50 Myr outburst is only sufficient to provide a simmering of the immediately surrounding gas. Nevertheless, this is adequate to raise the energy in the gas which can be transported through weak shocks and magnetohydrodynamic waves into the entire cluster medium on a ten times longer time scale in between the outbursts. Repeated bursts then act to raise the energy until the simmering gas is able to effectively cool and a cooling inflow develops. Without the repeated gentle simmering, the radio burst would blow away the cluster medium. This implies that the cluster cooling flows we now see

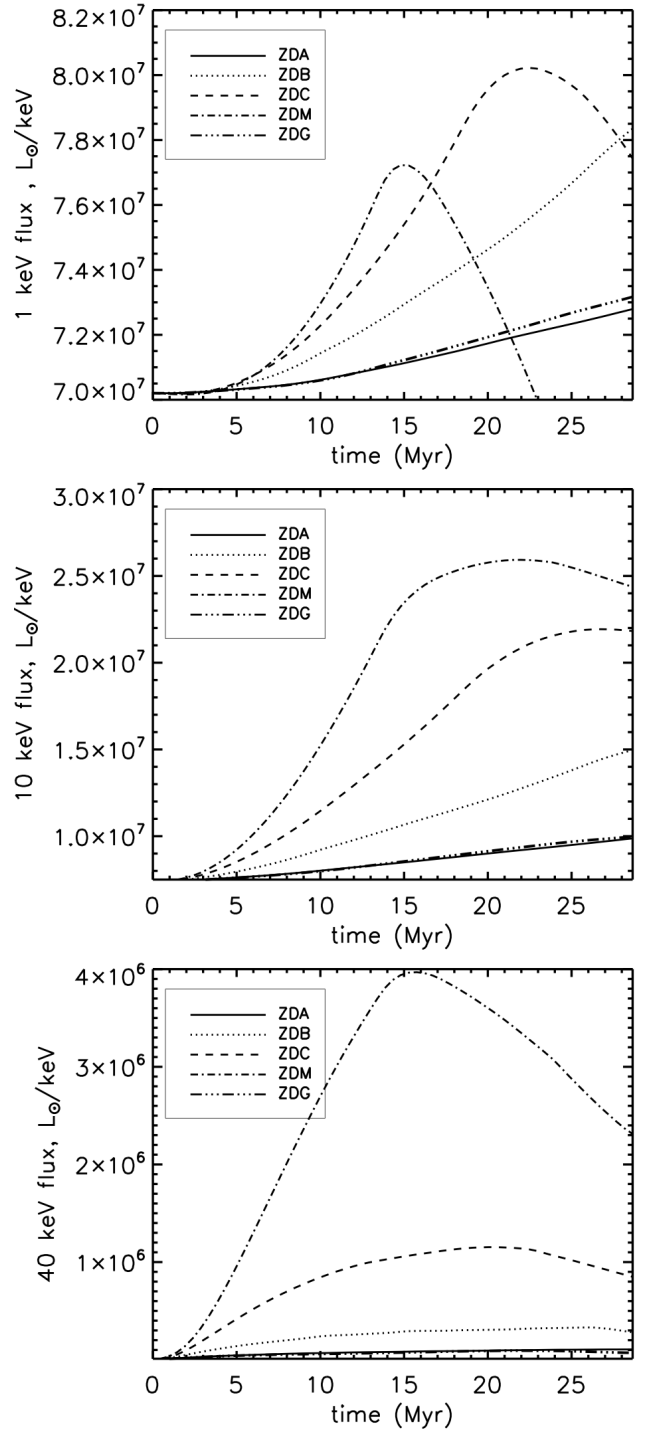


**Figure 15.** Evolution of the flux density. The total X-ray emission in each band of spectral width 1 keV over the entire 150 kpc cube as a function of time.

as strong X-ray sources have reached the point of balance between the simmering process and the radiative cooling.

## 5 CONCLUSIONS

We have presented simulated X-ray images of radio galaxies formed through supersonic hydrodynamic jets. Only synchrotron



and thermal Bremsstrahlung processes have been considered without consideration for radiative losses or particle acceleration. Three dimensional simulations are necessary not only for the precession but also for the correct form of dissipation of turbulent energy through cascade downwards in wavelength.

Standard Mach 6 jets drive shells and cavities of roughly ellipsoidal shape and show a decrement in surface brightness of at most a few tens of per cent. We have found that both cavities/shells and bows/arcs are generated in the soft and hard X-ray bands, respectively.

Straight FR II jets are associated with elliptical shells when the jet-ambient density ratio is high and with (projected as triangular) conical X-ray lobes when the jets are very light. Remarkable thick rib structures are evident when the jet-ambient density ratio is near 0.01.

Precession generates bi-lobed or X-shaped radio sources and in curved or deflected radio jets. In these cases, the strongest X-ray emission is found to be not associated with the hotspot but with the relic lobe or deflection location. This is because the regions of hot high-pressure gas and regions of dense high-compression do not coincide. As the viewing angle is changed towards the line of sight, the cavity becomes a deep round hole surrounded by circular ripples.

Low Mach number shocks extend into the cluster environment but a single episode of radio galaxy formation is not sufficient for long-term support of a cooling flow. We have found that the total radio luminosity of a simulated radio galaxy does not increase with source age or size. This is because the integrated emission is dominated by the higher pressure regions which are of relatively constant volume, rather than the low pressure lobes. The jet kinetic power is mainly transferred into the ambient medium via shocks and compression as shown in Paper 1. In contrast, the X-ray luminosity steadily increases, especially in the higher energy bands, until ambient gas is expelled from the simulated region.

A new result is the appearance of a rib cage in soft X-rays which may be related to the structure found in Cygnus A as presented in detail from Chandra observations (Duffy et al. 2018). We have only considered thermal X-ray emission in this work and so have investigated the shape of cavities. It should also be noted that inverse Compton losses to photons from the Cosmic Microwave Background may well dominate the X-ray image as well as alter the radio structure and the morphological type as the relative contributions of the hotspot and diffuse lobe may systematically change (Ker et al. 2012). Furthermore, a non-thermal X-ray jet in Cygnus A is mis-aligned from the radio jet suggesting a precession scenario (Steenbrugge et al. 2008). Relativistic jet flows are generally expected to yield similar flow patterns but light travel time effects may introduce new details. However, X-ray properties should not be altered. As noted above, the relativistic electrons which generate the radio emission are a source of energy which is transferred to cosmic microwave background photons via inverse Compton scattering throughout the lobes. This can fill in the cavities and reduce the number of radio galaxies which display cavities.

Finally, using 3C 310 as an example, we demonstrate that a radio galaxy is efficient at simmering the intracluster medium. A periodic gentle heating over several short episodes could support the external medium through the propagation of weak shocks.

These conclusions are founded on several model assumptions. We assume a uniform ambient medium which will evidently never be the case and rarely valid as an approximation. The density within isolated galaxies and clusters are observed to decrease with distance from the bulge or core for nearby examples (Croston et al.

2008). Moreover, for the distant radio galaxies being considered here, the propensity of progressing galaxy and cluster mergers are found to significantly disturb the density profiles and X-ray structures (Bartalucci et al. 2017).

Adopting a non-uniform radial profile would have a profound influence on precessing jets as has been found for the near straight jet variety (Clarke et al. 1997). The jet would progress from light to heavy and the corresponding dominant radio structure change from the artist's brush to a ballistic pattern in which the jet path is delineated. For the external X-ray emission, the cocoon would become broader as the radio galaxy penetrates into less dense fields. This reduces the emission from the bow caps and creates considerably more open X-ray cavity structures, as often observed and simulated (Krause 2005).

In addition, it should be reiterated that we also assume no active influence from a magnetic field in either medium, non-relativistic speeds, no shear or spray on exit from the jet nozzle and an initial thermal pressure balance on entry. All these assumptions will be tested in future works.

## 6 ACKNOWLEDGEMENTS

We wish to thank SEPnet for supplying infrastructure funding.

## 7 DATA AVAILABILITY

Data available on request. The data underlying this article will be shared on reasonable request to the corresponding author.

## REFERENCES

- Akahori T., et al., 2020, *PASJ*, **72**, 62  
 Atoyan A., Dermer C. D., 2004, *ApJ*, **613**, 151  
 Bartalucci I., Arnaud M., Pratt G. W., Démoclès J., van der Burg R. F. J., Mazzotta P., 2017, *A&A*, **598**, A61  
 Belsole E., Worrall D. M., Hardcastle M. J., Croston J. H., 2007, *MNRAS*, **381**, 1109  
 Bîrzan L., Rafferty D. A., McNamara B. R., Wise M. W., Nulsen P. E. J., 2004, *ApJ*, **607**, 800  
 Bîrzan L., et al., 2020, *MNRAS*, **496**, 2613  
 Boehringer H., Voges W., Fabian A. C., Edge A. C., Neumann D. M., 1993, *MNRAS*, **264**, L25  
 Carilli C. L., Perley R. A., Harris D. E., 1994, *MNRAS*, **270**, 173  
 Choi Y.-Y., Reynolds C. S., Heinz S., Rosenberg J. L., Perlman E. S., Yang J., 2004, *ApJ*, **606**, 185  
 Clarke D. A., Harris D. E., Carilli C. L., 1997, *MNRAS*, **284**, 981  
 Croston J. H., et al., 2008, *A&A*, **487**, 431  
 Croston J. H., Hardcastle M. J., Mingo B., Evans D. A., Dicken D., Morganti R., Tadhunter C. N., 2011, *ApJ*, **734**, L28  
 Donohoe J., Smith M. D., 2016, *MNRAS*, **458**, 558  
 Duffy R. T., et al., 2018, *MNRAS*, **476**, 4848  
 Fabian A. C., 2012, *ARA&A*, **50**, 455  
 Giacintucci S., et al., 2011, *ApJ*, **732**, 95  
 Guo F., 2015, *ApJ*, **803**, 48  
 Gupta N., et al., 2020, *MNRAS*,  
 Hardcastle M. J., Krause M. G. H., 2013, *MNRAS*, **430**, 174  
 Hardcastle M. J., et al., 2019, *A&A*, **622**, A12  
 Jaffe W., Perola G. C., 1974, *A&A*, **31**, 223  
 Kataoka J., Stawarz Ł., 2005, *ApJ*, **622**, 797  
 Ker L. M., Best P. N., Rigby E. E., Röttgering H. J. A., Gendre M. A., 2012, *MNRAS*, **420**, 2644  
 Kraft R. P., et al., 2012, *ApJ*, **749**, 19

- Krause M., 2005, *A&A*, **431**, 45
- Krause M. G. H., et al., 2019, *MNRAS*, **482**, 240
- Mendygral P. J., O’Neill S. M., Jones T. W., 2011, *ApJ*, **730**, 100
- Mignone A., Bodo G., Massaglia S., Matsakos T., Tesileanu O., Zanni C., Ferrari A., 2007, *ApJS*, **170**, 228
- Pandge M. B., Vagshette N. D., David L. P., Patil M. K., 2012, *MNRAS*, **421**, 808
- Pandge M. B., Sonkamble S. S., Parekh V., Dabhade P., Parmar A., Patil M. K., Raychaudhury S., 2019, *ApJ*, **870**, 62
- Prasow-Émond M., et al., 2020, *AJ*, **160**, 103
- Riffel R. A., et al., 2019, *MNRAS*, **485**, 5590
- Rybicki G. B., Lightman A. P., 1979, *Radiative processes in astrophysics*
- Shin J., Woo J.-H., Mulchaey J. S., 2016, *ApJS*, **227**, 31
- Smith M. D., Donohoe J., 2019, *MNRAS*, **490**, 1363
- Smith M. D., Norman M. L., Winkler K.-H. A., Smarr L., 1985, *MNRAS*, **214**, 67
- Smith D. A., Wilson A. S., Arnaud K. A., Terashima Y., Young A. J., 2002, *ApJ*, **565**, 195
- Sonkamble S. S., Vagshette N. D., Pawar P. K., Patil M. K., 2015, *Ap&SS*, **359**, 21
- Stawarz Ł., et al., 2014, *ApJ*, **794**, 164
- Steenbrugge K. C., Blundell K. M., Duffy P., 2008, *MNRAS*, **388**, 1465
- Toro E. F., Spruce M., Speares W., 1994, *Shock Waves*, **4**, 25
- Tucker W., 1975, *Radiation processes in astrophysics*
- Turner R. J., Shabala S. S., 2020, *MNRAS*,
- Vagshette N. D., Naik S., Patil M. K., Sonkamble S. S., 2017, *MNRAS*, **466**, 2054
- Vagshette N. D., Naik S., Patil M. K., 2019, *MNRAS*, **485**, 1981
- Wilson A. S., Yang Y., 2002, *ApJ*, **568**, 133
- Wilson A. S., Smith D. A., Young A. J., 2006, *ApJ*, **644**, L9
- Yarza R., Wong G. N., Ryan B. R., Gammie C. F., 2020, *ApJ*, **898**, 50